Spatiotemporal variations in atmospheric CH$_4$ concentrations and enhancements in northern China based on a comprehensive dataset: Ground-based observations, TROPOMI data, inventory data and inversions

Pengfei Han[1,2*], Ning Zeng[3], Bo Yao[4], Wen Zhang[5], Weijun Quan[6], Pucai Wang[2], Ting Wang[2], Minqiang Zhou[1,2], Qixiang Cai[7,8*], Yuzhong Zhang[9,10], Ruosi Liang[9,10], Wanqi Sun[11*], Shengxiang Liu[2,12]

[1]Key Laboratory of Atmospheric Environment and Extreme Meteorology, Institute of Atmospheric Physics, Chinese Academy of Sciences, Beijing 100029, China

[2]Carbon Neutrality Research Center, Institute of Atmospheric Physics, Chinese Academy of Sciences, Beijing, China

[3]Department of Atmospheric and Oceanic Science, and Earth System Science Interdisciplinary Center, University of Maryland, College Park, Maryland, USA

[4]Department of Atmospheric and Oceanic Sciences and Institute of Atmospheric Sciences, Fudan University, Shanghai, China

[5]State Key Laboratory of Atmospheric Boundary Layer Physics and Atmospheric Chemistry, Institute of Atmospheric Physics, Chinese Academy of Sciences, Beijing, China

[6]Institute of Urban Meteorology (Key Laboratory of Urban Meteorology), China Meteorological Administration, Beijing, China

[7]State Key Laboratory of Numerical Modeling for Atmospheric Sciences and Geophysical Fluid Dynamics, Institute of Atmospheric Physics, Chinese Academy of Sciences, Beijing, China

[8]Qiluzhongke Institute of Carbon Neutrality, Jinan, China

[9]Key Laboratory of Coastal Environment and Resources of Zhejiang Province, School of Engineering, Westlake University, Hangzhou, Zhejiang, China

[10]Institute of Advanced Technology, Westlake Institute for Advanced Study, Hangzhou, Zhejiang, China

[11]Meteorological Observation Centre, China Meteorological Administration, Beijing, China

[12]Jiujiang University, Jiujiang, Jiangxi, China

Correspondence to: Pengfei Han (pfhan@mail.iap.ac.cn); Qixiang Cai (caiqixiang@mail.iap.ac.cn);

Wanqi Sun (sunwanqi2008@126.com)

Abstract. Methane (CH_4) is a potent greenhouse gas with a global warming potential that is 28–36-fold higher than that of CO_2 at the 100-year scale. Northern China notably contributes to CH_4 emissions. However, high uncertainties remain in emissions, and observation gaps exist in this region, especially in urban areas. Here, we compiled a comprehensive dataset (available at https://doi.org/10.5281/zenodo.10957950) (Han et al., 2024), including ground- and satellite-based observations, inventory data and modeling results, to study the CH_4 concentration, enhancement and spatiotemporal variation in this area. High-precision in situ observations from Beijing and Xianghe revealed that obvious seasonal cycles and notable enhancements (500–1500 ppb) occurred at a regional background site (Shangdianzi). We found significant increasing trends in the CH_4 concentration over time in both the ground- and satellite-based observations and positive correlations between these observations. Anthropogenic emissions largely contributed to surface concentration variations and their increases in middle and southern Shanxi Province and northern Hebei Province. However, a spatially inconsistent pattern was observed between the results of optimized simulations driven by surface atmospheric inversion data and Tropospheric Monitoring Instrument (TROPOMI) column CH_4 observations in summer. Further validation on the basis of this comprehensive dataset indicated that the TROPOMI data may exhibit systematic bias in summer. The posterior concentrations generally agreed well with the surface in situ observations (mean biases ranging from -2.3~80.7 ppb). The posterior surface CH_4 concentrations (with a spatial resolution of $0.5° \times 0.625°$) revealed that southern Shanxi, northern Henan, and Beijing exhibited relatively high levels (an increase of ~300 ppb), which were positively correlated with the PKU-CH_4-v2 emission inventory data. This study provides a comprehensive dataset of CH_4 concentrations and enhancements in high-emission areas, which can benefit the research community and policy-makers for designing future observations, conducting atmospheric inversions and formulating policies.

Keywords: Methane, in situ measurements, TROPOMI, TCCON, emissions inventory; atmospheric inversions

1   Introduction

Methane (CH_4) is a potent greenhouse gas (GHG) that exhibits a 28–36-fold greater global warming

60   potential than that of CO_2 at the 100-year scale (Hu et al., 2024; Lin et al., 2021), with a radiative

forcing of 0.61 W m^{-2}, and CH_4 is responsible for almost one-third of the total warming to date

(Etminan et al., 2016; IPCC, 2022). According to National Oceanic and Atmospheric Administration

(NOAA) atmospheric observations, the global mean atmospheric CH_4 growth rate increased

dramatically to 13.2 ppb in 2022, resulting in record-high CH_4 levels above 1900 ppb throughout 2022

65   (https://gml.noaa.gov/ccgg/trends_ch4/). The fluctuations in the atmospheric CH_4 concentration are

driven by various natural (e.g., wetlands) and anthropogenic sources (e.g., fossil fuel exploitation), and

atmospheric CH_4 can be removed by sinks via chemical oxidation involving hydroxyl radicals (OH)

and dry soil sinks involving aerobic methane-oxidizing bacteria (Lin et al., 2021; Saunois et al., 2020;

Tan et al., 2022; Turner et al., 2019). Anthropogenic sources contribute approximately 60% to global

70   CH_4 emissions (Jackson et al., 2020; Saunois et al., 2020). Thus, reductions in anthropogenic CH_4

emissions have significant implications for achieving near-term climate goals (Gouw et al., 2020; IPCC,

2022; Staniaszek et al., 2022). To limit global warming to 1.5 ℃, more than 130 countries have pledged

to achieve carbon neutrality or net-zero emissions, which requires the combined reduction in both CO_2

and non-CO_2 (GHG) emissions (Fankhauser et al., 2022; Ou et al., 2021).

75   Emissions originating from urban areas account for approximately 21% of global CH_4 emissions (Zhao

et al., 2019). For example, Crippa et al. (2021) reported that urbanization contributed to a sixfold faster

increase in CH_4 emissions stemming from urban centers and that energy, transport, and waste were the

dominant drivers of increases in urban emissions. Since 2000, CH_4 emissions in China have rapidly

increased in response to industrialization and urbanization development (Lin et al., 2021).

80   Accompanying this trend, notable expanding hotspots in megacities and high-energy-exploitation

regions have become a concern. China enacted an ambitious plan to reach carbon neutrality before

2060 to address climate change. In November 2023, China issued the Methane Emissions Control

Action Plan, which targets a utilization volume of coal mine methane of 6 billion cubic meters, a

utilization rate of urban household waste of approximately 60%, and a utilization rate of dung and

85   waste from livestock of at least 80% by 2025 (MEE, 2023). Understanding the current emission status,

impacts on atmospheric CH_4 concentration increases, and mitigation potentials for CH_4 emissions are

prerequisites for developing effective mitigation policies.

Although previous efforts have been made to improve the accuracy of CH_4 emission estimates for China, substantial inconsistencies remain, especially in hotspot regions (Lin et al., 2021; Liu et al.,

90   2021b; Miller et al., 2019; Sheng et al., 2019). The recent emission inventories of PKU-CH_4 v2 (Liu et al., 2021b), Community Emissions Data System (CEDS) v2021-4-21 (Hoesly, 2019) and Emissions Database for Global Atmospheric Research (EDGAR) v7.0 (Crippa, 2023) exhibit a wide range of 47–67 Tg for 2019, which highlights the considerable uncertainty in the application of bottom-up methods. These uncertainties are due mainly to differences in source-specific emission factors and spatial

95   disaggregation of national or provincial annual totals (Crippa, 2023; Lin et al., 2021; Peng et al., 2016; Zhang et al., 2016). Furthermore, differences among inventories could substantially affect inversions using inventory data as prior estimates. The adoption of data from existing top-down studies (Miller et al., 2019; Yin et al., 2021) based on outdated bottom-up inventories could bias the determination of trends in CH_4 emissions in China (Liu et al., 2021b). Tan et al. (2022) also reported that the inversion

100   model performance is highly affected by prior data and measurements of trends across China. There is a pressing need to improve the accuracy of CH_4 emission estimates to support the implementation of mitigation strategies and better characterize regional CH_4 surface fluxes.

Satellite observational platforms provide promising pathways for tracking spatial and temporal variations in CH_4 sources (Irakulis-Loitxate et al., 2021; Jacob et al., 2016; Pandey et al., 2019; Schuit

105   et al., 2023; Turner et al., 2015). Satellite retrievals of the column-averaged dry air mole fraction of methane (XCH_4) with an unprecedented spatiotemporal coverage and resolution can be used to rapidly detect CH_4 variations and verify bottom-up inventories. Although several previous studies have involved the use of data from the Greenhouse Gases Observing Satellite (GOSAT) and the SCanning Imaging Absorption Spectrometer for Atmospheric Chemistry (SCIAMACHY) to characterize

110   atmospheric CH_4 concentrations in China, the monitoring of emissions originating from large sources remains limited because of the relatively sparse observations and coarse resolution (Chen et al., 2022a; Chen et al., 2022b; Tan et al., 2022). Furthermore, Plant et al. (2022), Maasakkers et al. (2022), and Peng et al. (2023) reported that inventoried urban CH_4 emissions are underestimated relative to Tropospheric Monitoring Instrument (TROPOMI)-based estimates. Several studies have shown the

115   ability of the recently launched TROPOMI to track and quantify CH_4 emissions stemming from point

and regional sources (Barré et al., 2021; Jacob et al., 2016; Schuit et al., 2023). Gouw et al. (2020) reported that the TROPOMI can identify distinct methane emission increases in oil and natural production regions in the United States. Liu et al. (2021c) developed a new divergence method to estimate CH_4 emissions in Texas (North America) on the basis of TROPOMI observations. Liang et al. (2023) used TROPOMI observations to estimate emissions in East Asia.

Northern China, encompassing the Beijing–Tianjin–Hebei (BTH) region and its surrounding provinces (including Shanxi, Shandong, Jiangsu, Anhui, and Henan), is a populous region with rapid socioeconomic development, and more than 30% of the anthropogenic CH_4 emissions in China in 2019 was generated in this region (PKU-CH_4, Fig. 1). Previous studies have indicated that northern China is a CH_4 emission hotspot region (Liang et al., 2023; Tan et al., 2022). Emissions resulting from the production of raw coal in northern China constitute one of the major sources, and Shanxi is the largest regional CH_4 emitter, yielding 5.7 Tg of emissions in 2019 (PKU-CH_4). Notably, northern China is a hotspot region for atmospheric CH_4 concentration and flux studies.

In this study, we used high-precision in situ observations, Total Carbon Column Observing Network (TCCON) observations, satellite data, inventory data, and modeling data from atmospheric inversions to better understand the spatiotemporal variations and spatial gradients of atmospheric CH_4 concentrations and the correlations between emissions and concentrations in northern China. On the basis of this comprehensive dataset, we aimed to (1) quantify the spatiotemporal CH_4 concentrations and enhancements in northern China; (2) study the correlations between satellite- and ground-based observations; and (3) assess the consistency and deviation in results derived from surface and satellite observations. First, we studied the temporal variations in local CH_4 concentrations and their enhancement in urban areas. Second, we analyzed the correlations between satellite-based column CH_4 concentrations and surface observations. Third, we assessed the model performance via high-precision measurements. Finally, we analyzed the spatial and temporal variations in posterior concentrations determined with the Westlake model, which exhibits a satisfactory output and performance, at the monthly, seasonal, and yearly scales.

2 Data and methods

2.1 Surface observations

To monitor GHG emissions in support of assessing the realization of carbon neutrality goals, China is
145   making great efforts in terms of its GHG monitoring capacity (Han et al., 2018; MEE, 2021; Sun et al.,
2022; Zeng et al., 2021). Three stations equipped with high-precision (1 ppb) Picarro instruments have
been established in the BTH region, namely, the urban Beijing station (BJ), the suburban Xianghe
station (XH), and the regional background Shangdianzi station (SDZ) (Fig. 1, Table 1), since 2019.
Wind rose plots for data from these sites are shown in Fig. S1. Moreover, two TCCON stations
150   (http://www.tccon.caltech.edu/), namely, the Hefei and Xianghe stations, were established to
continuously monitor the variability in the atmospheric XCH_4. In this study, we analyzed surface
measurements along with satellite observations to better understand the temporal variations and
seasonal cycles of atmospheric CH_4 from 2019 to 2021, while TCCON data were also employed to
assess TROPOMI observations.

155

Table 1 Information on the three regional high-precision observation sites

| Station name	Abbreviations	Station type	Longitude (°E)	Latitude (°N)	Altitude (m)	Height of the inlet (m)
Beijing	BJ	Urban	116.3667	39.9667	49	80/280
Xianghe	XH	Suburban	116.9578	39.7833	95	60/100
Shangdianzi	SDZ	Regional background	117.1166	40.6500	293	16/80

2.1.1 Ground-based high-precision in situ measurements

In situ measurements of atmospheric CH_4 dry mole fractions were conducted at the three sites (BJ, XH,
160   and SDZ) via Picarro GHG analyzers (Fig. 1). The BJ station (116.37°E, 39.97°N) is located at the
Institute of Atmospheric Physics, Chinese Academy of Sciences, in urban Beijing between the Third
and Fourth Ring Roads (Liu et al., 2021a). This area is densely populated, and CH_4 concentrations are
frequently influenced by local residential and transportation emissions. The XH station (39.75°N,
116.96°E) is located at a suburban site that represents the transition region from urban to regional

165   background areas (Yang et al., 2021). The SDZ station (117.12 °E, 40.65 °N) is one of the regional

Global Atmosphere Watch (GAW) stations of the World Meteorological Organization (WMO) in China

and occurs on a mountainside 100 km northeast of urban Beijing. There is a small village in the lower

valley of the mountain. The major vegetation types are shrubs and corn (Fang et al., 2016). The Mona

Loa (MLO, 19.54 °N, 155.58 °W) site is a GAW station representing the global background (not shown

170   in Fig. 1) located atop a mountain on Hawaii Island with the longest history of observations. The

background map in Fig. 1 shows 10 km×10 km gridded anthropogenic CH_4 emissions from the

PKU-CH_4 inventory with hotspots in Shanxi, Beijing, Henan, Anhui, and Inner Mongolia, while the

subplots show sectoral CH_4 emissions from 2000 to 2019 at the provincial scale (Figs. 1 and S2).
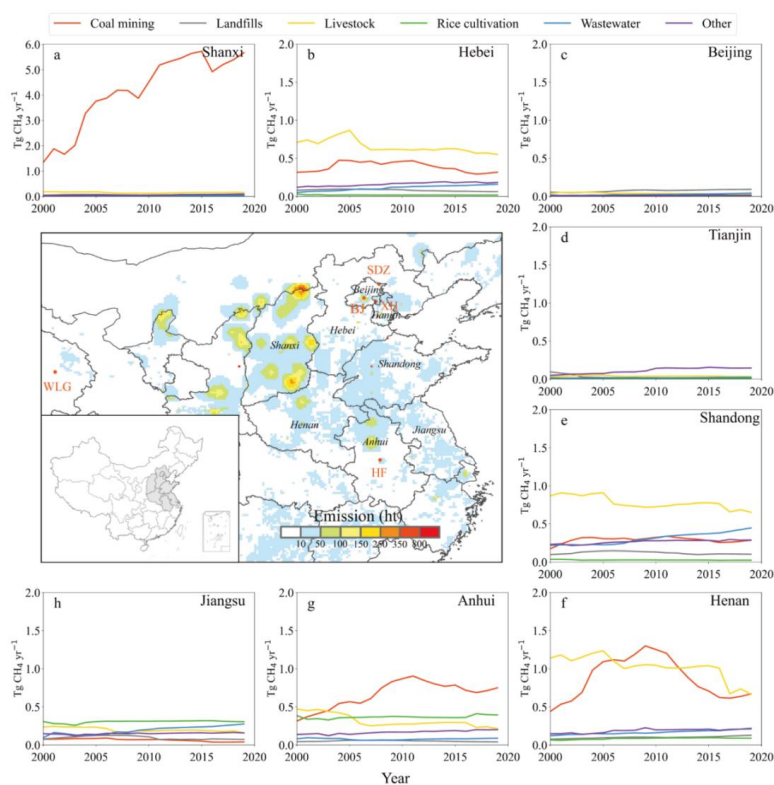
175   **Fig. 1 Observation sites (red dots) and gridded anthropogenic CH_4 emissions and sectoral emissions in**
northern China from the PKU-CH_4-v2 inventory.

Cavity ring-down spectroscopy (CRDS) instruments (Picarro G2301/G2401, Picarro Inc.) were used to

continuously measure in situ atmospheric CH_4 concentrations at BJ, XH and SDZ. CH_4 concentration

180   data from the Waliguan (WLG) and MLO sites were obtained from the World Data Center for

Greenhouse Gases (WDCGG; https://gaw.kishou.go.jp/). At the three regional sites, ambient air was

sampled by an oil-free vacuum pump at different tower levels after particles were removed with a 2-μm

filter. Then, the air was dried with a Nafion dryer to the dewpoint at –25°C, and the pressure and flow

rate were stabilized before the air samples were analyzed with a CRDS instrument. All the observation

185   systems were calibrated every 6 hours by WMO X2007 standard gases. The accuracy of the

observations was greater than 1 ppb at a 1-minute resolution. The sampling height was 80/280 m above

ground level at BJ, 60/100 m at XH, and 16/80 m at SDZ.

2.1.2 Ground-based total column measurements

The TCCON aims to measure column-average mole fractions of CO_2, CH_4, and other gases beginning

190   in 2004 across 30 sites worldwide via solar absorption spectroscopy in the near-infrared region

(Laughner et al., 2023). It is a ground-based network of Fourier transform spectrometers (FTSs)

designed to retrieve high-precision data on GHG emissions and to provide a validation dataset for

space-based measurements (Wunch et al., 2011; Wunch et al., 2010). Here, we used GGG2020 TCCON

data from the Hefei (HF, 117.17°E, 31.9°N) and XH stations (Liu, 2023; Zhou, 2022). A

195   high-resolution FTS (IFS125HR, Bruker GmbH, Germany) system and a solar tracker (Tracker-A Solar

547, Bruker GmbH, Ettlingen, Germany) have been installed at the HF site since January 2014 (the site

location shown in Fig. 1) (Wang et al., 2017). The observatory is located in the northwestern suburbs of

Hefei and is surrounded by wetlands and croplands (Tian et al., 2018). Therefore, the CH_4

concentration observed at the HF station may be partly influenced by local anthropogenic emissions

200   from urban areas and cultivated lands and by natural emissions from wetlands (Tian et al., 2018; Wang

et al., 2017). The bias correction factor for CH_4 at HF is 0.9765, with a 1σ standard deviation of 0.0020

(Tian et al., 2018). Additionally, an automatic weather station (ZENO 3200, Coastal Environmental

Systems, Inc., Seattle, USA) was installed near the solar tracker instrument on the roof in September

2015 to collect meteorological data (Shan et al., 2019; Wang et al., 2017). The other TCCON site is

205   located at XH in the suburban area 50 km southeast of Beijing (Zhou et al., 2023). The XH station is

surrounded by croplands and residential buildings (with an average height of ~20 m) (Yang et al., 2021).

A Bruker IFS 125HR instrument was installed in the upper level of a four-story building in June 2016,

and a solar tracker instrument was installed on the rooftop in June 2018 (Yang et al., 2021). The

retrieved XCH$_4$ products at XH are subjected to air-mass-dependence correction and calibrated to the

210   WMO scale (Wunch, 2015; Yang et al., 2020).

2.2 Satellite observations

The TROPOMI onboard the Copernicus Sentinel-5 Precursor is a nadir-viewing, imaging spectrometer

covering wavelength bands between the ultraviolet and shortwave infrared (SWIR) bands (Veefkind et

al., 2012). The TROPOMI retrieves a methane column from the 2305–2385-nm SWIR band and the

215   757–774-nm near-infrared band, with a daily global coverage at a fine spatial resolution of 5.5 km×7

km since August 2019 (7 km×7 km from January to August 2019) and a swath width of ∼2600 km

(Butz et al., 2012; Hu et al., 2016; Lorente et al., 2021). We used the TROPOMI CH$_4$ total column level

2 data product to quantify the variations and trends in northern China from January 2019 to December

2021. We employed XCH$_4$ retrievals with quality values greater than 0.5 (Gouw et al., 2020). To ensure

220   comparison with surface measurements, bottom-up inventories and inversion results at different spatial

resolutions, the TROPOMI XCH$_4$ observations were averaged to three spatial resolutions of 0.1 °×0.1 °,

0.25 °×0.25 °, and 0.5 °×0.5 °. The TROPOMI data were resampled to each of the spatial resolutions. We

first defined the spatial bounds of the resampled grids and then placed the original pixels into coarser

grids according to the longitude and latitude of the pixel center. We defined the resampled values of

225   XCH$_4$ as the average of the original pixels belonging to the new resampled grids. This method ensures

consistency between the regionally averaged XCH$_4$ values before and after resampling, with an average

relative error of 0.03%. We used TCCON data from HF and XH to evaluate the accuracy and precision

of the TROPOMI observations.

2.3 Bottom-up inventory

230   A gridded inventory of anthropogenic CH$_4$ emissions from Peking University (PKU-CH$_4$ v2) (Liu et al.,

2021b; Peng et al., 2023; Peng et al., 2022), which has been assessed in our previous study (Lin et al.,

2021), was adopted in this study. PKU-CH$_4$ v2 is an annual bottom-up inventory based on provincial

activity data and regional, sector-specific emission factors for eight major sectors in China (Liu et al.,

2021b; Peng et al., 2016). The inventory provides a priori knowledge of the temporal and regional

235   distribution characteristics of anthropogenic CH$_4$ emissions in China. The main sources of CH$_4$

emissions in China are coal mining and agriculture, which contributed approximately 77% to the total

national emissions in 2019 (Lin et al., 2021; Liu et al., 2021b).

Coal mining is the dominant driver of CH_4 emissions in China, accounting for >80% of the increase in the total emissions in the 2000s due to the growth in coal production with rapid economic development

240   and the increasing energy demand (Lin et al., 2021; Liu et al., 2021b). However, the reductions in both coal production and emission factors, with increasing utilization rates, contributed to slowing coal methane emissions from 2010–2019 (Liu et al., 2021b).

2.4 Atmospheric modeling and inversions

We employed the GEOS-Chem model as the forward model and an analytical Bayesian method for

245   inversions to optimize a state vector x containing annual methane emissions from 600 clusters and average methane column biases at four model boundaries covering East Asia (Liang et al., 2023), and Westlake data were considered optimized concentration data, with a spatial resolution of 0.5 °×0.625 °. TROPOMI XCH_4 observations were used for data assimilation purposes. The former is a combined product. For oil and gas, we used the Global Fuel Exploitation Inventory (GFEI) v1.0 dataset, and for

250   coal in China, we used the inventory of Sheng et al. (2019), while the data for other sectors were derived from the EDGAR v4.3.2 dataset (Janssens-Maenhout et al., 2019). To consider major patterns in the distribution of emissions and significantly reduce the inversion computation burden, emissions were optimized on the basis of 600 spatial clusters instead of the native 0.5 °×0.625 ° grid, which were generated with a Gaussian mixed model algorithm (Turner and Jacob, 2015). The model performance

255   was evaluated by high-precision in situ observations. The optimized surface and column concentrations were used to analyze the spatiotemporal dynamics of CH_4 concentrations and emissions. Moreover, Copernicus Atmosphere Monitoring Service (CAMS) global inversion-optimized greenhouse gas concentrations were used in the comparison, which are coarse-resolution (2 °×3 °) monthly data that can provide a regional baseline (Rayner et al., 2016).

260

3   Results and discussion

3.1 Temporal variations in the in situ CH_4 concentrations and enhancements in urban areas determined by ground-based high-precision measurements

To determine the importance of understanding the uncertainties in concentrations and emissions in the

265 study area, we firstly analyzed the temporal variations and the spatial enhancements on the basis of

ground-based observations. There were clear temporal variations in the high-precision in situ CH_4

concentrations (Fig. 2) at all three sites from the urban BJ station to the suburban XH station to the

regional background SDZ station. The concentrations at BJ and XH ranged from ~2000 ppb for the

baseline to 4000–5000 ppb for the peak values in September and January in some heavily polluted

270 cases in winter. These results could be associated with high emissions from nearby wetlands at XH in

summer and high residential and natural gas power plant emissions at BJ in winter (Ji et al., 2020).

Such high concentrations have also been observed in large cities in Canada and the U.S., such as Los

Angeles (Verhulst et al., 2017), Washington, D.C., and Baltimore (Huang et al., 2019), and Indianapolis

(Mitchell et al., 2022). Furthermore, the WLG site (green line) provided a continental baseline, while

275 the MLO site (red line) provided a global baseline. There were also notable seasonal cycles and high

spatial gradients at the three regional sites (Figs. 2 and 3, respectively). In contrast, SDZ and WLG

exhibited fewer seasonal cycles.
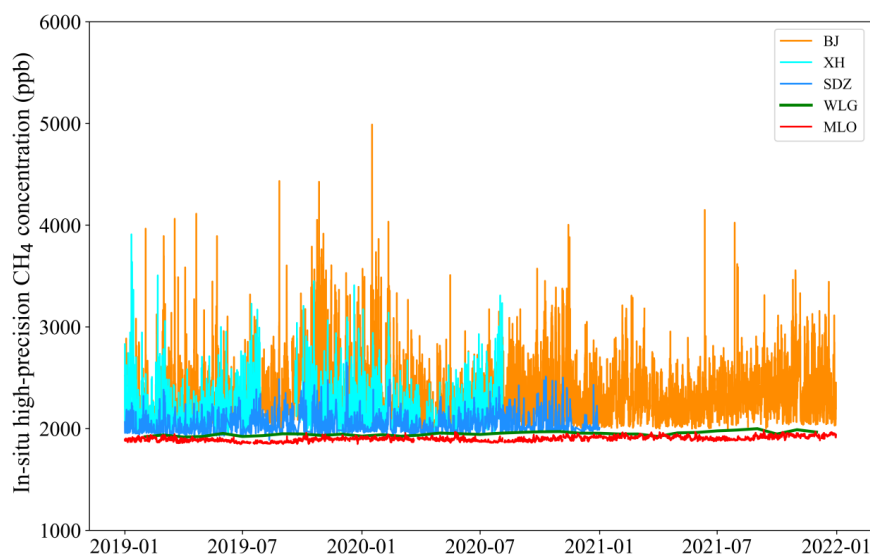
Fig. 2 Hourly CH_4 variations at the four sites in northern China on the basis of ground high-precision

280 **observations. For WLG, we used weekly data because of data availability.**

11
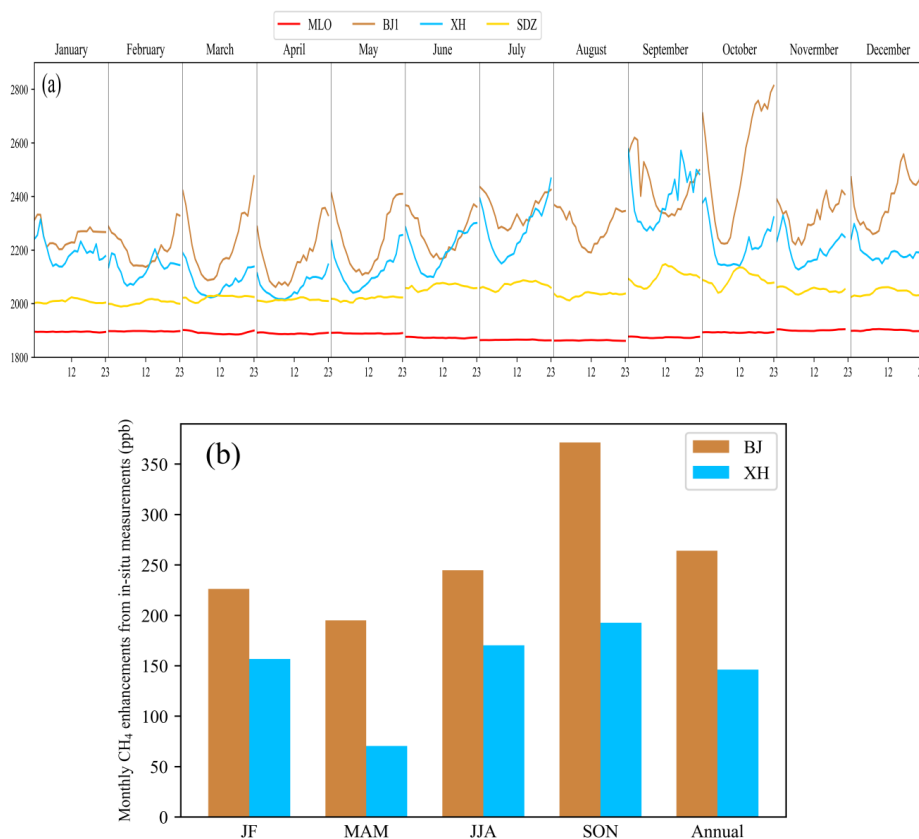
Fig. 3 Enhancements in the in situ CH$_4$ concentrations at BJ and XH compared with that at SDZ for the hourly mean from 00:00–23:59 (UTC time) in each month (Panel a) and during the four seasons and for the annual mean (Panel b) in 2019.

For the CH$_4$ enhancements in urban and suburban areas, the urban BJ station exhibited the greatest enhancements, with an annual mean enhancement ranging from 200–350 ppb over the 2019 season (Fig. 3a and b), followed by the suburban XH station (with seasonal enhancements ranging from 50–200 ppb), compared with the concentration at the regional background SDZ station. The jumps during the months shown in Fig. 3a occurred because the hourly means from 23:00–23:59 within a certain month differed from those from 00:00–00:59 within the next month. The MLO data revealed the lowest surface concentrations (~1800 ppb) and provided a global-scale background. The three regional sites all exhibited obvious enhancements over the MLO. The CH$_4$ dome observed in northern China is comparable to that observed in other cities in Canada and the USA, such as Los Angeles (Verhulst et

al., 2017) and Washington, D.C. (Huang et al., 2019), but higher than that observed in Salt Lake City and Toronto, with values ranging from 100–1000 ppb (Mitchell et al., 2022). These surface enhancements also exhibited seasonal cycles, with higher values in autumn (371 and 193 ppb at BJ and XH, respectively) and lower signals in spring (195 and 70 ppb at BJ and XH, respectively). Moreover,

300 the monthly enhancements were consistent with this trend, with high enhancements from September to November (Fig. S3). In addition, the diurnal cycle was obvious each month, with a convex curve mostly influenced by the planetary boundary layer height (PBLH), which is similar to that of CO_2 (Bao et al., 2020) and air pollutants (Chu et al., 2019; Su et al., 2018).

305 **3.2 Correlations between the satellite-based XCH$_4$ concentrations and surface observations**

Satellite observations have an advantage in spatial coverage, yet they need careful calibrations and validations, especially for regional scale studies. The satellite and surface observations generally agreed well in capturing seasonal variations, the CH_4 concentration was highest in autumn, and the concentration decreased to a low level in winter (Fig. 4). The phase of the cycles in the seasonal

310 column CH_4 concentrations at BJ, XH, and SDZ from the TROPOMI data was consistent with that of the surface in situ measurements at the monthly scale (Fig. 4a, b and Fig. S4). However, the in situ CH_4 concentrations were greatly influenced by local emissions and meteorological conditions, with larger amplitudes than those of the TROPOMI data, thus yielding lower correlations with XCH$_4$ (R^2=0.16 and 0.48, for p<0.05 and 0.01 at BJ and SDZ, respectively; Fig. 5a, b). Furthermore, the urban BJ station

315 exhibited higher XCH$_4$ values than those at the suburban XH station and the regional background SDZ station, which is consistent with the surface in situ measurements with higher signals. These results also indicated high local anthropogenic emissions in the urban areas of Beijing. At HF, the average XCH$_4$ was highest from August–September because of emissions originating from surrounding wetlands and rice paddies (Figs. 4d and 1). BJ and SDZ exhibited the highest values from September–October.
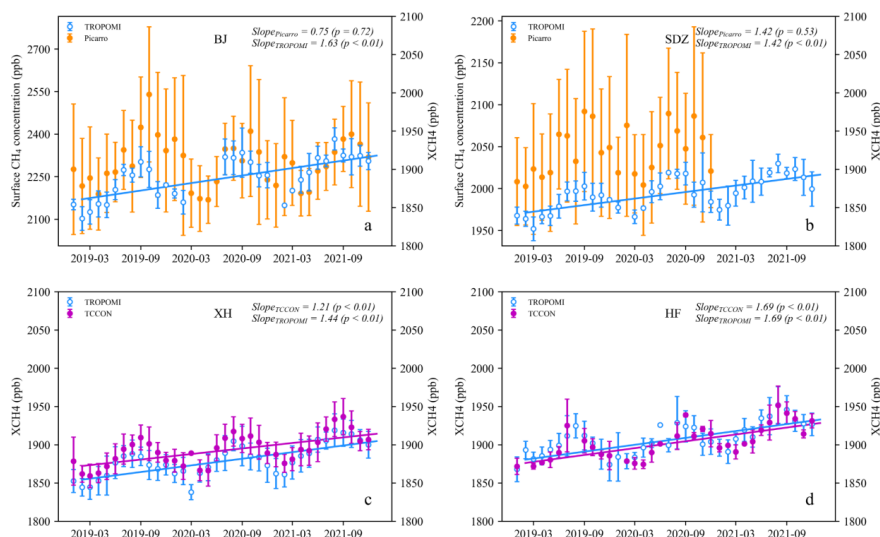
Fig. 4 Temporal variations in the mean monthly XCH₄ and surface CH₄ concentrations observed at the BJ (a), SDZ (b), XH (c), and HF (d) stations from 2019–2021. Note that the scales differ between BJ and SDZ.

As expected, the phase and magnitude of the seasonal cycles observed in the TROPOMI data at XH and HF better agreed with those in the TCCON data than did the in situ comparisons (Fig. 4), with higher variations in the in situ observations (Fig. 4a, b). The R^2 values were 0.76 and 0.75 for XH and HF (Fig. 5c, d), respectively, which are higher than those with the in situ observations (Fig. 5a, b), with a p value <0.01 at both sites.

Moreover, there were seasonal trends between the TROPOMI and TCCON observations, with positive biases in the TROPOMI observations in spring and summer (5–15 ppb, or 0.5%) and negative biases in winter (~-5 ppb, or 0.25%) compared with the higher-precision TCCON observations, which is consistent with the findings of Sha et al. (2021). The TROPOMI XCH₄ and Hefei TCCON XH₂O values were significantly positively correlated, with $R^2 = 0.43$ and a p value <0.01 (Fig. 6b). Similar results have also been reported in other studies. High CH₄ biases at high latitudes correlated with H₂O columns were found in H₂O retrievals from the TROPOMI by Schneider et al. (2020) and Lorente et al. (2021). The satellite retrieval biases might also be associated with cloudiness in summer and thus the limited number of TROPOMI observations (Qu et al., 2021) and relevant surface albedo and scattering issues (Barré et al., 2021; Schneising et al., 2023; Schneising et al., 2019). Moreover, we calculated the

XCH$_4$ and in situ CH$_4$ growth rates. The XCH$_4$ level observed from the TROPOMI data clearly

340 increased from 2019–2021, with increase rates ranging from 1.4 to 1.6 ppb month^{-1} ($p < 0.01$, Fig. 4).

Future TROPOMI validations for potential H$_2$O impacts need vertical profile observations in southern

area (e.g. in Anhui and Henan Province) in summer.
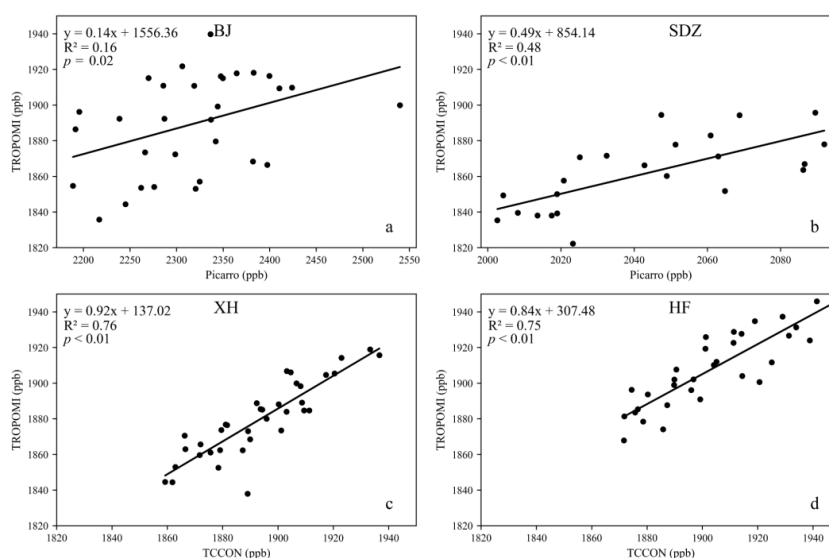
Fig. 5 Correlations between the mean monthly XCH$_4$ concentration from the TROPOMI dataset and the surface CH$_4$ concentration observed at BJ (a) and SDZ (b) and correlations between the mean monthly XCH$_4$ concentrations from the TROPOMI and TCCON datasets at XH (c) and HF (d) from 2019–2021.
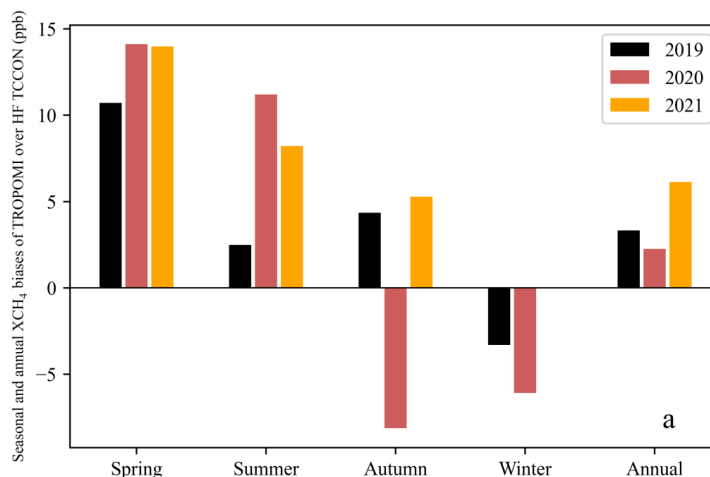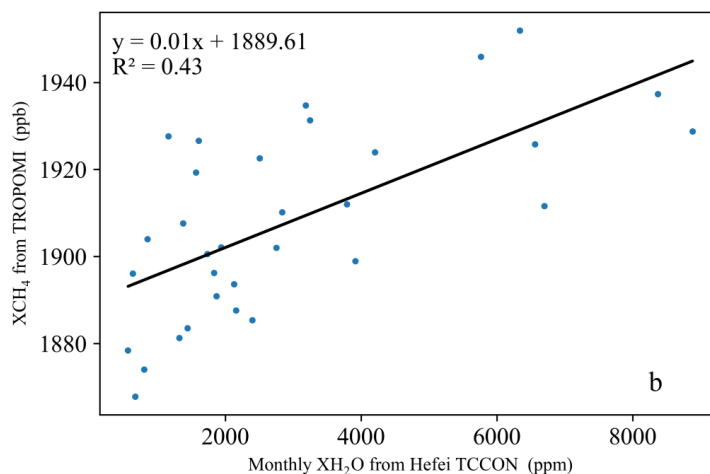
Fig. 6 (a) Seasonal and annual biases of the TROPOMI XCH$_4$ observations minus the Hefei TCCON observations from 2019–2021. (b) Positive correlations between the monthly XH$_2$O from the Hefei TCCON observations and XCH$_4$ from the TROPOMI observations.

3.3 Validation of the model performance against in situ measurements

To assess the accuracy of the posterior CH$_4$ data from the GEOS-Chem and CAMS models, we compared the simulated concentrations with the high-precision measurements at BJ, XH, and SDZ. We used the mean bias (MB) and root mean square error (RMSE) to assess the model performance. The MB is an indicator of systematic biases, while the RMSE reflects the spread in simulations with higher weights for large errors. In general, the models captured the CH$_4$ trends and variations (Figs. 7 and 8, respectively). The daily comparisons between the simulations and observations revealed a negative bias at the urban BJ site (MB=-57.2 ppb) and positive biases at the XH (77.4 ppb) and SDZ (68.0 ppb) sites (Fig. 8). The optimized GEOS-Chem model captured the observed baseline at BJ (Fig. 7a) but slightly overestimated the baselines at XH and SDZ (Fig. 7b, c and Fig. 8). Moreover, the RMSEs for the three sites decreased from the urban BJ site (185.6 ppb) to the suburban XH site (157.7 ppb) and the regional background SDZ site (110.7 ppb) (Fig. 8). The simulations could not capture some of the peak values in urban Beijing (Fig. 7a), indicating considerable simulation challenges in urban areas with complex anthropogenic emissions, which is consistent with the CO$_2$ and air pollutant simulations (Feng et al., 2019; Liang et al., 2022).

370   The seasonal and annual biases of the GEOS-Chem and CAMS models relative to the in situ

measurements were calculated (Fig. 8). Both models showed negative biases (-39 ~ -152 ppb) from

spring to autumn in Beijing and positive biases (17~86 ppb) in winter, which was due to the higher

baseline simulations on clean days (Fig. 8a). The GEOS-Chem model simulations revealed positive

biases in the annual mean at the suburban and regional background sites during most seasons (Fig. 8b,

375   c). The CAMS model showed positive biases at XH and negative biases at SDZ, and both sites showed

positive biases in winter (Fig. 8b, c). The hourly and monthly comparisons also revealed similar

variations and trends (Figs. S5 and S6, respectively), while the monthly and seasonal data from the

CAMS model also revealed negative biases in urban areas and positive biases in suburban areas, with

lower biases at the suburban and regional background sites than at the urban site (Figs. 8c and S6).
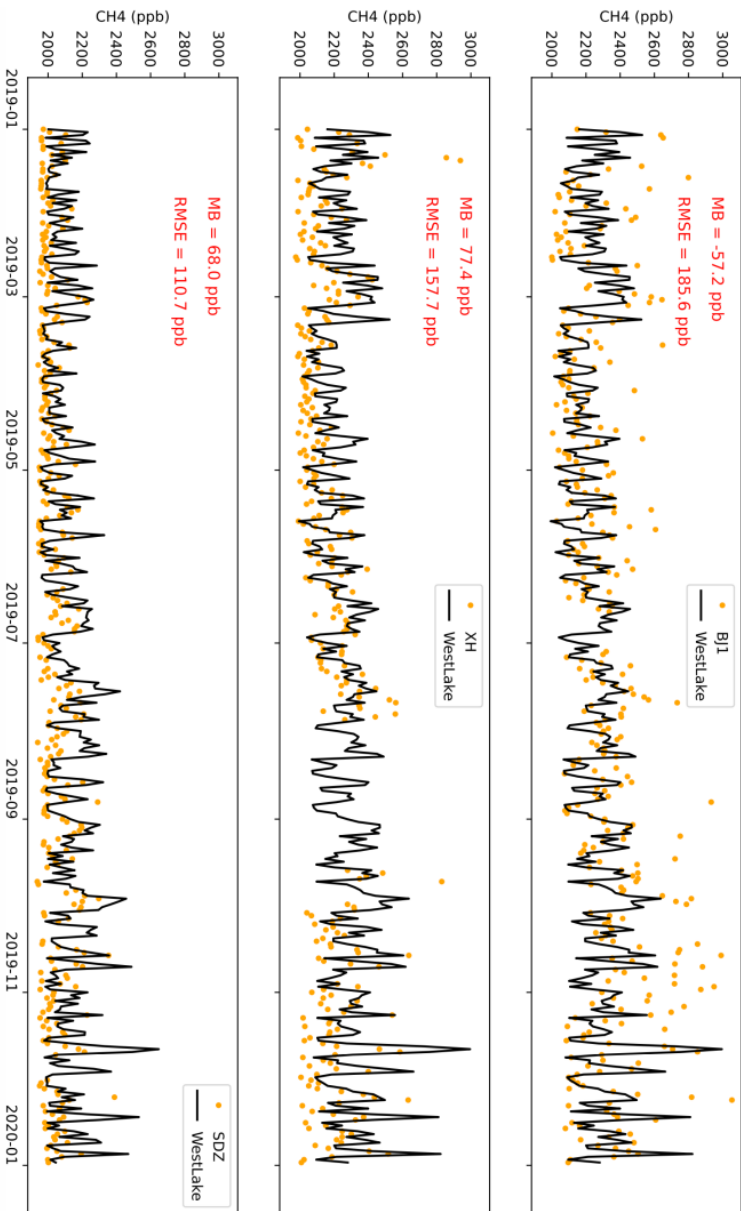
380

Fig. 7 Daily comparisons of the Westlake model simulations with the in situ high-precision measurements at the three sites. MB denotes the mean bias, and RMSE is the mean root square error. BJ, XH, and SDZ denote the observations from the Beijing, Xianghe, and Shangdianzi stations, respectively.
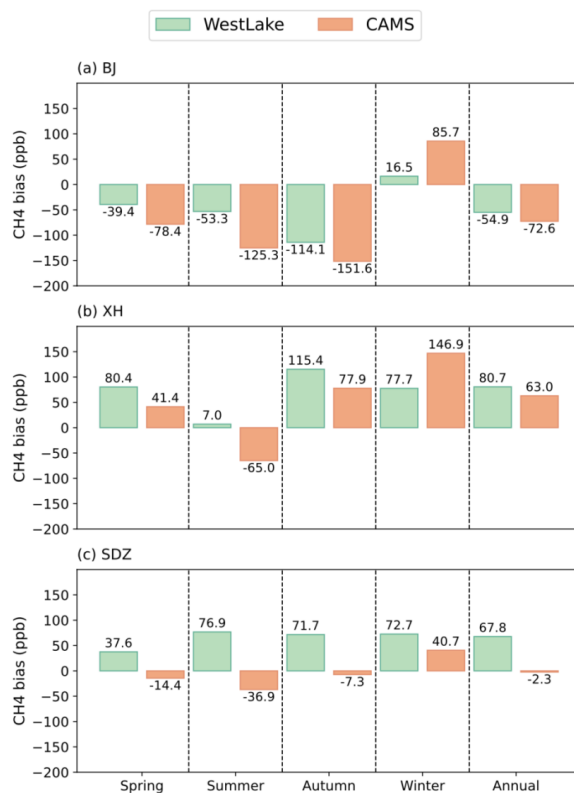
18

385

Fig. 8 Seasonal and annual biases for the Westlake and CAMS models compared with the high-precision in situ measurements.

390   **3.4 Spatial characteristics of the inversion-optimized surface CH₄ concentrations and their correlations with emissions**

Northern China serves as a notable CH$_4$ source, and the total emissions increased to 14.2 Tg yr^{-1} in 2019 (Figs. 1 and S2), accounting for 30% of the total emissions in China (Liu et al., 2021b). Correspondingly, the optimized GEOS-Chem model surface CH$_4$ concentration reached 2112.1 ppb in

395   2019. High surface concentrations were mostly consistent with high emissions in southern Shanxi, northern Henan, Hebei and Beijing (Figs. 9–11 and Fig. 1), which has also been reported by Peng et al. (2023) in Shanxi. In contrast, most parts of Shandong, Jiangsu and Anhui indicated a relatively low

annual mean concentration in 2019. In terms of seasonal and monthly spatial patterns, spring (March–April–May) exhibited the lowest values, while autumn (September–October–November) and winter

400   (January–February) exhibited much higher concentrations (Figs. 9 and 10, respectively). The northern part demonstrated lower concentrations in winter than in summer, largely due to the favorable climatic conditions for dispersion, with greater wind speeds in winter than during the other seasons (Figs. 9 and 10). We also compared the Westlake column CH_4 data with the TROPOMI observations, and these two datasets exhibited consistent spatial patterns across all seasons (Fig. S7) and suitable correlations

405   (R^2=0.72~0.85, $p < 0.01$; Fig. S8).

Moreover, the spatial patterns of the surface and column concentrations revealed inconsistent trends in spring (March–April–May) and summer (June–July–August) (Figs. 10 and S9, respectively), and the p values for the negative correlations during both seasons were less than 0.01 (Fig. S10), which may be caused by the dynamic seasonal vertical profiles and potential influences of water vapor. Further

410   evidence from direct in situ vertical observations is needed. This phenomenon, in which the inverted surface concentrations are not positively correlated with the column concentrations, even indicating negative correlations in summer, must be investigated further via in situ profile observations.
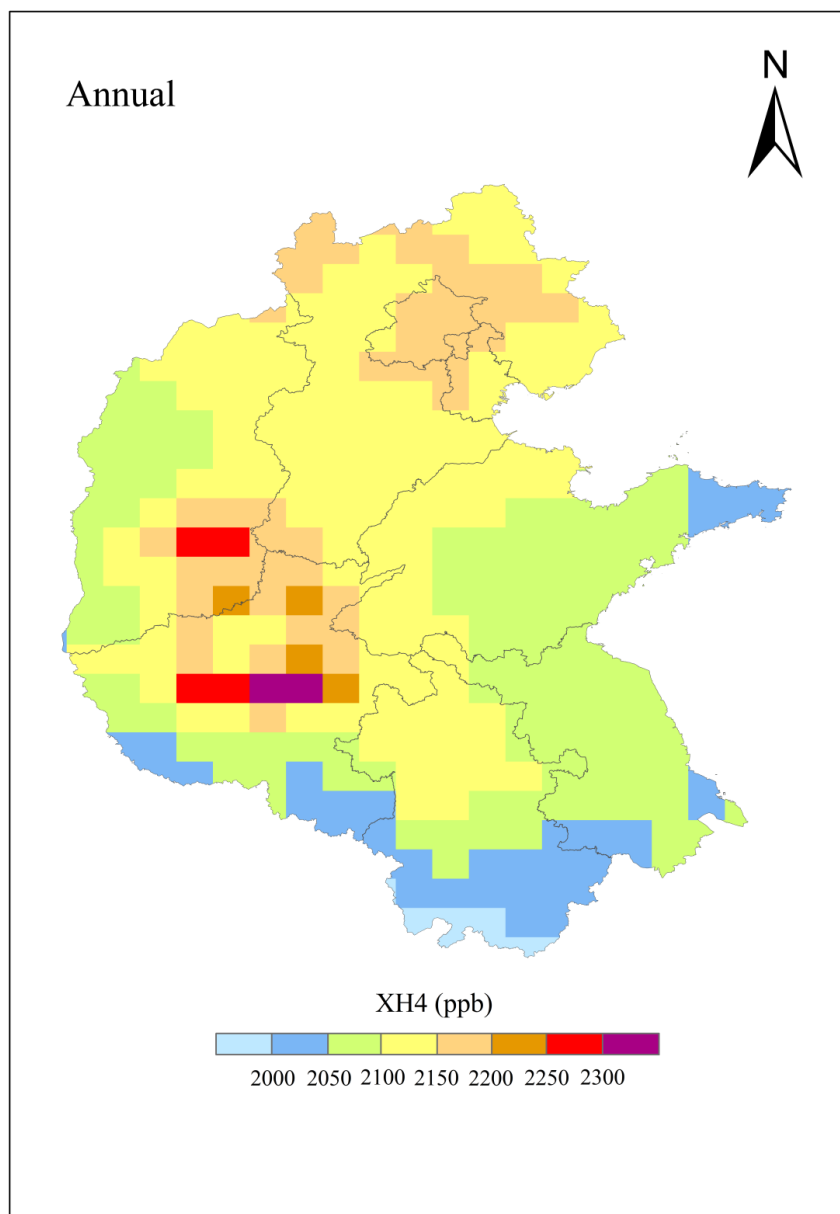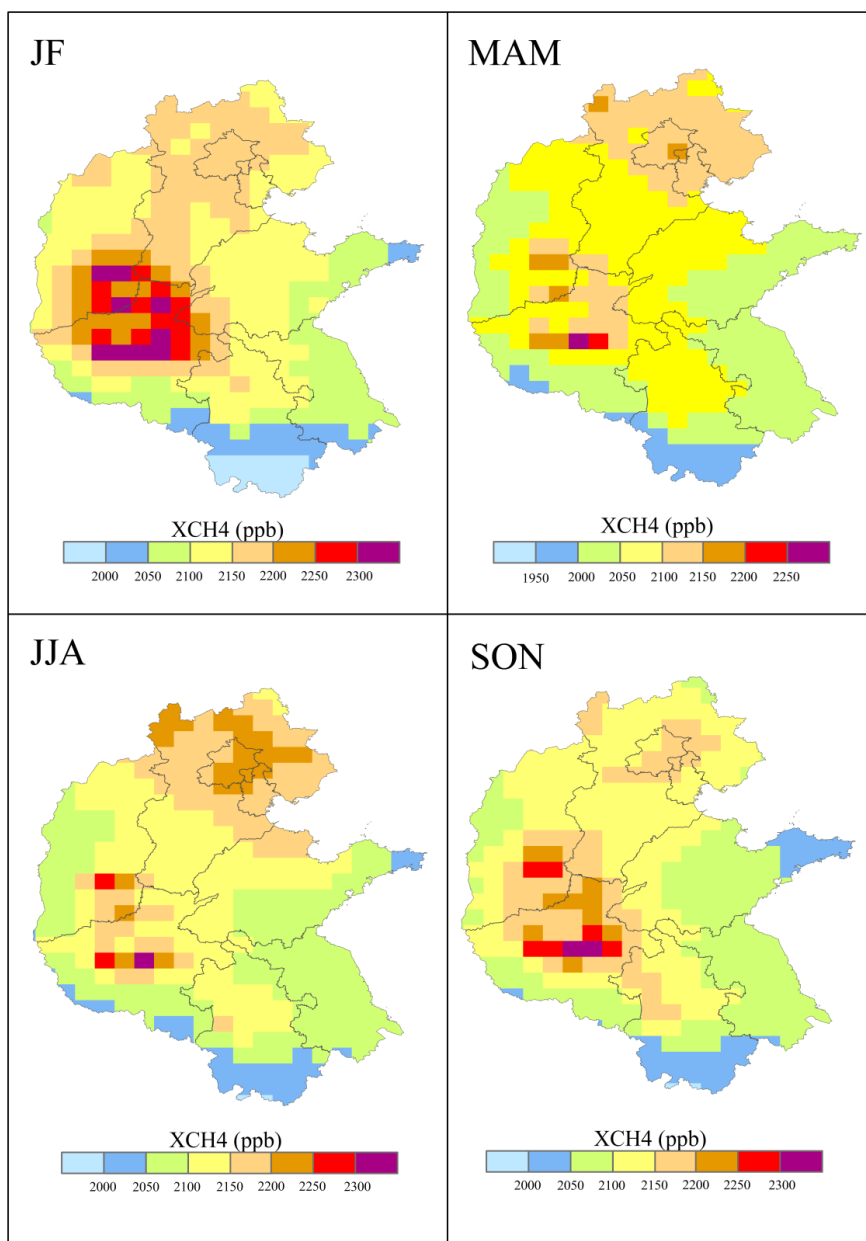
Fig. 9 Posterior annual and seasonal spatial distributions of the surface CH$_4$ concentration (Westlake) in northern China in 2019.
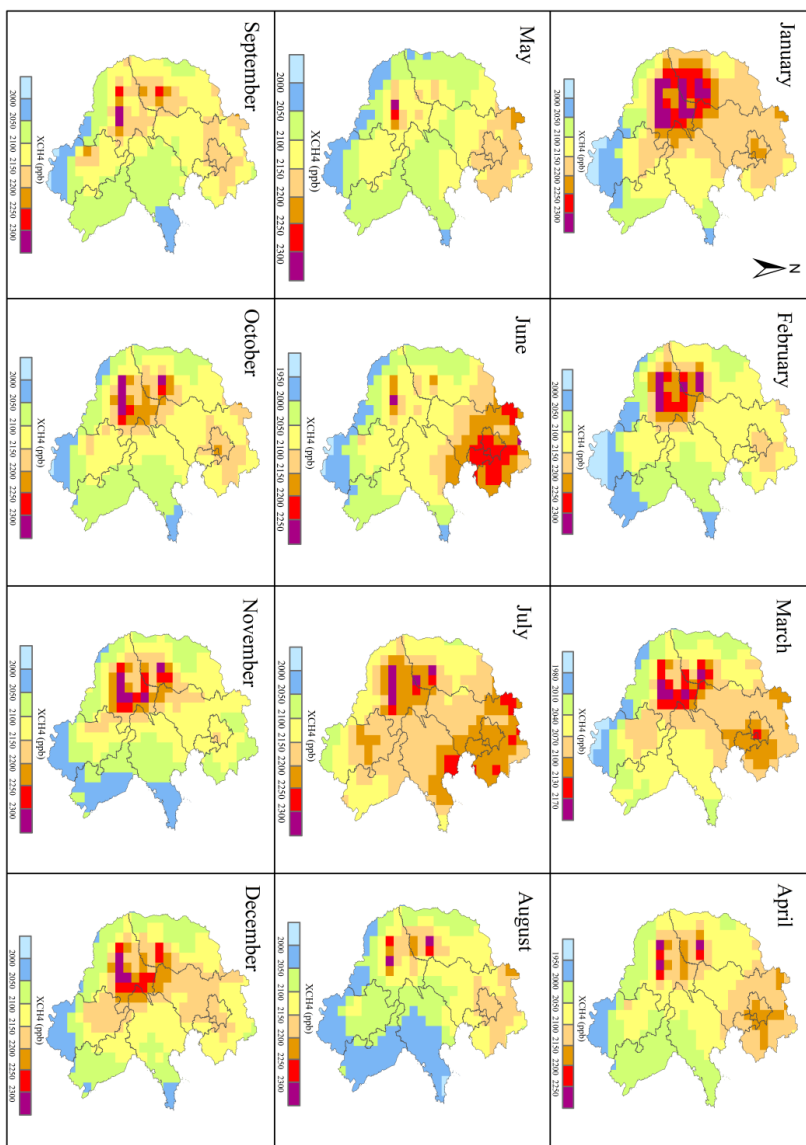
Fig. 10 Posterior monthly spatial distributions of the surface CH₄ concentration (Westlake) in northern China in 2019.

420   Enhanced surface CH_4 concentrations are an indication of high local emissions associated with coal

mining, oil and gas activities, agriculture, or wetland processes (Barré et al., 2021; Gouw et al., 2020;

Zhang et al., 2020). The correlation between the PKU emissions and the simulated surface

concentrations at the grid level (Fig. 11) was statistically significant ($p<0.05$), albeit with a low R^2

value of 0.06. Positive relationships with low R^2 have also been found in oil and gas production regions

425   in the U.S. (Gouw et al., 2020).
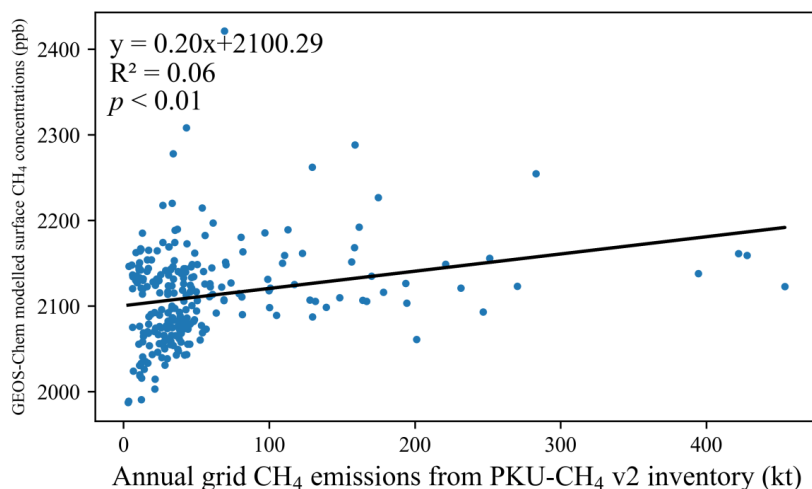

Fig. 11 Correlations between the CH_4 emissions and the PKU-CH_4-v2- and Westlake-modeled surface CH_4 concentrations.

430

Moreover, we found a positive correlation between the TROPOMI column CH_4 and PKU-CH_4-v2

emission inventories in Shanxi (Fig. S11), which demonstrates the ability of satellite data to detect

large local sources, such as coal mining (Peng et al., 2023), in urban regions. Recent studies have also

indicated that TROPOMI data combined with other satellite observations can be employed to identify

435   large emission sources in gas and oil well blowouts (Cusworth et al., 2021; Schuit et al., 2023). These

findings showed the potential use of satellite data in detecting hotspot emissions that may be omitted

from emissions inventory, and thus further mobile observations (e.g. cars and UAVs) can be used for

field double check in environmental enforcement.

4   Conclusions

440   In this study, we compiled a comprehensive dataset to study the spatiotemporal characteristics of surface and column CH_4 concentration variations and their correlations with emissions. We found that surface CH_4 concentrations can be much greater (500–1500 ppb) than regional background CH4 concentrations in urban and suburban areas because of anthropogenic emissions. Notable seasonal surface enhancements of 200–350 ppb at urban Beijing station and 50–200 ppb at the suburban

445   Xianghe station were observed compared with the concentration at the regional background Shangdianzi station. Positive relationships were found between the surface (both in situ and TCCON) and TROPOMI column observations. The inversion-optimized concentrations generally agreed well with the surface in situ observations in terms of the seasons and annual means in 2019. The optimized surface CH_4 concentrations were relatively high in southern Shanxi, northern Henan, and Beijing (with

450   enhancements of ~300 ppb), whereas relatively low concentrations were observed in southern Anhui and most parts of Jiangsu, which was positively correlated with the PKU-CH_4-v2 emission inventory data. However, the optimized surface concentrations were not positively correlated with the column concentrations and even indicated negative correlations in summer. Further investigations are needed to obtain column concentration algorithms and validate the in situ profile observations. This study

455   provides a comprehensive dataset of CH_4 concentrations and spatial gradients in northern China, which provides key data for further observations, atmospheric inversions and policy-making related to emission reduction.

460   **Supporting information**

Sectoral CH_4 emissions at the provincial level and simulated posterior monthly mean CH_4 concentrations, enhancements, etc., are contained in the Supporting information.

Data availability statement

The data used to generate the figures in this manuscript are available as open-access data at

465   https://doi.org/10.5281/zenodo.10957950 (Han et al., 2024).

Competing interests

The authors declare that they have no conflicts of interest.

Author contributions

PFH, QXC and WQS conceived and designed the study. PFH, QXC, RSL, WQS, and SXL collected
and analyzed the datasets. PFH led the writing of the paper, with contributions from all coauthors. All
coauthors contributed to the descriptions and discussions in the manuscript.

480   **Acknowledgments**

485 **References**

486 Bao, Z., Han, P., Zeng, N., et al., 2020. Observation and modeling of vertical carbon dioxide
487 distribution in a heavily polluted suburban environment. Atmospheric and Oceanic
488 Science Letters 13, 371 - 379.

489 Barré, J., Aben, I., Agustí-Panareda, A., et al., 2021. Systematic detection of local CH4 anomalies
490 by combining satellite measurements with high-resolution forecasts. Atmos. Chem. Phys.
491 21 (6), 5117-5136.

492 Butz, A., Galli, A., Hasekamp, O., et al., 2012. TROPOMI aboard Sentinel-5 Precursor: Prospective
493 performance of CH4 retrievals for aerosol and cirrus loaded atmospheres. Remote
494 Sensing of Environment 120, 267-276.

495 Chen, D., Chen, A., Hu, X., et al., 2022a. Historical trend of China's CH4 concentrations and
496 emissions during 2003–2020 based on satellite observations, and their implications.
497 Atmospheric Pollution Research 13 (12), 101615.

498 Chen, Z., Jacob, D.J., Nesser, H., et al., 2022b. Methane emissions from China: a high-resolution
499 inversion of TROPOMI satellite observations. Atmos. Chem. Phys. 22 (16), 10809-10826.

500 Chu, Y., Li, J., Li, C., et al., 2019. Seasonal and diurnal variability of planetary boundary layer height
501 in Beijing: Intercomparison between MPL and WRF results. Atmospheric Research 227,
502 1-13.

503 Crippa, M., Guizzardi, D., Pisoni, E., et al., 2021. Global anthropogenic emissions in urban areas:
504 patterns, trends, and challenges. Environmental Research Letters 16 (7), 074033.

505 Crippa, M.G., Diego; Pagani, Federico; Pisoni, Enrico, 2023. GHG Emissions at sub-national level.
506 European Commission, Joint Research Centre (JRC) [Dataset]
507 doi:10.2905/D67EEDA8-C03E-4421-95D0-0ADC460B9658 PID:
508 http://data.europa.eu/89h/d67eeda8-c03e-4421-95d0-0adc460b9658, accessed on
509 17th January 2024.

510 Cusworth, D.H., Duren, R.M., Thorpe, A.K., et al., 2021. Multisatellite Imaging of a Gas Well
511 Blowout Enables Quantification of Total Methane Emissions. Geophysical Research
512 Letters 48 (2), e2020GL090864.

513 Etminan, M., Myhre, G., Highwood, E.J. and Shine, K.P., 2016. Radiative forcing of carbon dioxide,
514 methane, and nitrous oxide: A significant revision of the methane radiative forcing.
515 Geophysical Research Letters 43, 12,614 - 12,623.

516 Fang, S., Tans, P.P., Dong, F., Zhou, H.-g. and Luan, T., 2016. Characteristics of atmospheric CO2
517 and CH4 at the Shangdianzi regional background station in China. Atmospheric
518 Environment 131, 1-8.

519 Fankhauser, S., Smith, S.M., Allen, M., et al., 2022. The meaning of net zero and how to get it right.
520 Nature Climate Change 12 (1), 15-21.

521 Feng, T., Zhou, W., Wu, S., et al., 2019. High-resolution simulation of wintertime fossil fuel CO2 in
522 Beijing, China: Characteristics, sources, and regional transport. Atmospheric Environment
523 198, 226-235.

524 Gouw, J.A.d., Veefkind, J.P., Roosenbrand, E., et al., 2020. Daily Satellite Observations of Methane
525 from Oil and Gas Production Regions in the United States. Scientific Reports 10 (1), 1379.

526 Han, P., Zeng, N., Wang, Y., et al., 2018. Regional carbon monitoring for the Beijing-Tianjin-Hebei
527 (JJJ) City Cluster. 20th EGU General Assembly, EGU2018, Proceedings from the

528   conference held 4-13 April, 2018 in Vienna, Austria, p.4149.

529   Han, P., Zeng, N., Yao, B., et al., 2024. Methane concentration and emissions data for the northern
530   China. [Zenodo]. Available at https://doi.org/10.5281/zenodo.10957950, last accessed on
531   April 11th 2024.

532   Hoesly, R., O'Rourke, P., Braun, C., Feng, L., Smith, S. J., Pitkanen, T., Seibert, J. J., Vu, L., Presley, M.,
533   Bolt, R., Goldstein, B., and Kholod, N., 2019. Community Emissions Data System (Version
534   Dec-23-2019), Zenodo, https://doi.org/10.5281/zenodo.3592073, Accessed on 17th
535   January 2024.

536   Hu, H., Chen, J., Zhou, F., et al., 2024. Relative increases in CH_4 and CO_2 emissions from wetlands
537   under global warming dependent on soil carbon substrates. Nature Geoscience 17 (1),
538   26-31.

539   Hu, H., Hasekamp, O., Butz, A., et al., 2016. The operational methane retrieval algorithm for
540   TROPOMI. Atmos. Meas. Tech. 9 (11), 5423-5440.

541   Huang, Y., Kort, E.A., Gourdji, S.M., et al., 2019. Seasonally resolved excess urban methane
542   emissions from the Baltimore/Washington, DC metropolitan region. Environmental
543   science & technology.

544   IPCC, 2022. Climate Change 2022: Impacts, Adaptation, and Vulnerability. Contribution of
545   Working Group II to the Sixth Assessment Report of the Intergovernmental Panel on
546   Climate Change [H.-O. Pörtner, D.C. Roberts, M. Tignor, E.S. Poloczanska, K. Mintenbeck,
547   A. Alegría, M. Craig, S. Langsdorf, S. Löschke, V. Möller, A. Okem, B. Rama (eds.)].
548   Cambridge University Press. Cambridge University Press, Cambridge, UK and New York,
549   NY, USA, 3056 pp., doi:10.1017/9781009325844.

550   Irakulis-Loitxate, I., Guanter, L., Liu, Y.-N., et al., 2021. Satellite-based survey of extreme methane
551   emissions in the Permian basin. Science Advances 7 (27), eabf4507.

552   Jackson, R.B., Saunois, M., Bousquet, P., et al., 2020. Increasing anthropogenic methane emissions
553   arise equally from agricultural and fossil fuel sources. Environmental Research Letters 15
554   (7), 071002.

555   Jacob, D.J., Turner, A.J., Maasakkers, J.D., et al., 2016. Satellite observations of atmospheric
556   methane and their value for quantifying methane emissions. Atmos. Chem. Phys. 16 (22),
557   14371-14396.

558   Janssens-Maenhout, G., Crippa, M., Guizzardi, D., et al., 2019. EDGAR v4. 3.2 Global Atlas of the
559   three major greenhouse gas emissions for the period 1970–2012. Earth System Science
560   Data 11 (3), 959-1002.

561   Ji, D., Zhou, M., Wang, P., et al., 2020. Deriving Temporal and Vertical Distributions of Methane in
562   Xianghe Using Ground-based Fourier Transform Infrared and Gas-analyzer
563   Measurements. Adv Atmos Sci 37 (6), 597-607.

564   Laughner, J.L., Toon, G.C., Mendonca, J., et al., 2023. The Total Carbon Column Observing
565   Network's GGG2020 Data Version. Earth Syst. Sci. Data Discuss. 2023, 1-86.

566   Liang, R., Zhang, Y., Chen, W., et al., 2023. East Asian methane emissions inferred from
567   high-resolution inversions of GOSAT and TROPOMI observations: a comparative and
568   evaluative analysis. Atmos. Chem. Phys. 23 (14), 8039-8057.

569   Liang, Z., Tang, W., Zeng, N., et al., 2022. High-precision observation and WRF model simulation
570   of surface atmospheric CO_2 concentration in Beijing-Tianjin-Hebei region (in Chinese).
571   Transactions of Atmospheric Sciences 45 (3), 387-396.

572   Lin, X., Zhang, W., Crippa, M., et al., 2021. A comparative study of anthropogenic CH4 emissions
573   over China based on the ensembles of bottom-up inventories. Earth Syst. Sci. Data 13 (3),
574   1073-1088.
575   Liu, C.W., W.; Sun, Y.; Shan, C., 2023. TCCON Data from Hefei (PRC), Release GGG2020.R1.
576   https://doi.org/10.14291/tccon.ggg2020.hefei01.R1.
577   Liu, D., Sun, W., Zeng, N., et al., 2021a. Observed decreases in on-road CO2 concentrations in
578   Beijing during COVID-19 restrictions. Atmos. Chem. Phys. 21 (6), 4599-4614.
579   Liu, G., Peng, S., Lin, X., et al., 2021b. Recent Slowdown of Anthropogenic Methane Emissions in
580   China Driven by Stabilized Coal Production. Environmental Science & Technology
581   Letters.
582   Liu, M., van der A, R., van Weele, M., et al., 2021c. A New Divergence Method to Quantify
583   Methane Emissions Using Observations of Sentinel-5P TROPOMI. Geophysical Research
584   Letters 48 (18), e2021GL094151.
585   Lorente, A., Borsdorff, T., Butz, A., et al., 2021. Methane retrieved from TROPOMI: improvement of
586   the data product and validation of the first 2 years of measurements. Atmos. Meas. Tech.
587   14 (1), 665-684.
588   Maasakkers, J.D., Varon, D.J., Elfarsdóttir, A., et al., 2022. Using satellites to uncover large methane
589   emissions from landfills. Science Advances 8 (32), eabn9683.
590   MEE, M.o.E.a.E.o.t.P.s.R.o.C., 2021. Carbon monitoring and assessment pilot work programme (in
591   Chinese).   Available   at
592   https://www.mee.gov.cn/ywdt/spxw/202109/t20210923_952715.shtml , accessed on
593   17th January 2024.
594   MEE, M.o.E.a.E.o.t.P.s.R.o.C., 2023. Methane emissions control action plan (in Chinese). Available
595   at https://www.mee.gov.cn/xxgk2018/xxgk/xxgk03/202311/t20231107_1055437.html ,
596   accessed on 17th January 2024.
597   Miller, S.M., Michalak, A.M., Detmers, R.G., et al., 2019. China's coal mine methane regulations
598   have not curbed growing emissions. Nature Communications 10 (1), 303.
599   Mitchell, L.E., Lin, J.C., Hutyra, L.R., et al., 2022. A multi-city urban atmospheric greenhouse gas
600   measurement data synthesis. Scientific Data 9 (1), 361.
601   Ou, Y., Roney, C., Alsalam, J., et al., 2021. Deep mitigation of CO2 and non-CO2 greenhouse
602   gases toward 1.5 °C and 2 °C futures. Nature Communications 12 (1), 6245.
603   Pandey, S., Gautam, R., Houweling, S., et al., 2019. Satellite observations reveal extreme methane
604   leakage from a natural gas well blowout. Proceedings of the National Academy of
605   Sciences 116 (52), 26376-26381.
606   Peng, S., Giron, C., Liu, G., et al., 2023. High-resolution assessment of coal mining methane
607   emissions by satellite in Shanxi, China. iScience 26 (12), 108375.
608   Peng, S., Lin, X., Thompson, R.L., et al., 2022. Wetland emission and atmospheric sink changes
609   explain methane growth in 2020. Nature 612 (7940), 477-482.
610   Peng, S., Piao, S., Bousquet, P., et al., 2016. Inventory of anthropogenic methane emissions in
611   mainland China from 1980 to 2010. Atmos. Chem. Phys. 16, 14545-14562.
612   Plant, G., Kort, E.A., Murray, L.T., Maasakkers, J.D. and Aben, I., 2022. Evaluating urban methane
613   emissions from space using TROPOMI methane and carbon monoxide observations.
614   Remote Sensing of Environment 268, 112756.
615   Qu, Z., Jacob, D.J., Shen, L., et al., 2021. Global distribution of methane emissions: a comparative

616   inverse analysis of observations from the TROPOMI and GOSAT satellite instruments.
617   Atmos. Chem. Phys. 21 (18), 14159-14175.
618 Rayner, P., Michalak, A.M. and Chevallier, F., 2016. Fundamentals of Data Assimilation. Geosci.
619   Model Dev. Discuss. 2016, 1-21.
620 Saunois, M., Stavert, A.R., Poulter, B., et al., 2020. The Global Methane Budget 2000–2017. Earth
621   Syst. Sci. Data 12 (3), 1561-1623.
622 Schneider, A., Borsdorff, T., aan de Brugh, J., et al., 2020. First data set of H2O/HDO columns from
623   the Tropospheric Monitoring Instrument (TROPOMI). Atmos. Meas. Tech. 13 (1), 85-100.
624 Schneising, O., Buchwitz, M., Hachmeister, J., et al., 2023. Advances in retrieving XCH4 and XCO
625   from Sentinel-5 Precursor: improvements in the scientific TROPOMI/WFMD algorithm.
626   Atmos. Meas. Tech. 16 (3), 669-694.
627 Schneising, O., Buchwitz, M., Reuter, M., et al., 2019. A scientific algorithm to simultaneously
628   retrieve carbon monoxide and methane from TROPOMI onboard Sentinel-5 Precursor.
629   Atmos. Meas. Tech. 12 (12), 6771-6802.
630 Schuit, B.J., Maasakkers, J.D., Bijl, P., et al., 2023. Automated detection and monitoring of methane
631   super-emitters using satellite data. Atmos. Chem. Phys. 23 (16), 9071-9098.
632 Sha, M.K., Langerock, B., Blavier, J.F.L., et al., 2021. Validation of methane and carbon monoxide
633   from Sentinel-5 Precursor using TCCON and NDACC-IRWG stations. Atmos. Meas. Tech.
634   14 (9), 6249-6304.
635 Shan, C., Wang, W., Liu, C., et al., 2019. Regional CO emission estimated from ground-based
636   remote sensing at Hefei site, China. Atmospheric Research 222, 25-35.
637 Sheng, J., Song, S., Zhang, Y., Prinn, R.G. and Janssens-Maenhout, G., 2019. Bottom-Up Estimates
638   of Coal Mine Methane Emissions in China: A Gridded Inventory, Emission Factors, and
639   Trends. Environmental Science & Technology Letters 6 (8), 473-478.
640 Staniaszek, Z., Griffiths, P.T., Folberth, G.A., et al., 2022. The role of future anthropogenic methane
641   emissions in air quality and climate. npj Climate and Atmospheric Science 5 (1), 21.
642 Su, T., Li, Z. and Kahn, R., 2018. Relationships between the planetary boundary layer height and
643   surface pollutants derived from lidar observations over China: regional pattern and
644   influencing factors. Atmos. Chem. Phys. 18 (21), 15921-15935.
645 Sun, Y., Yin, H., Wang, W., et al., 2022. Monitoring greenhouse gases (GHGs) in China: status and
646   perspective. Atmos. Meas. Tech. 15 (16), 4819-4834.
647 Tan, H., Zhang, L., Lu, X., et al., 2022. An integrated analysis of contemporary methane emissions
648   and concentration trends over China using in situ and satellite observations and model
649   simulations. Atmos. Chem. Phys. 22 (2), 1229-1249.
650 Tian, Y., Sun, Y., Liu, C., et al., 2018. Characterisation of methane variability and trends from
651   near-infrared solar spectra over Hefei, China. Atmospheric Environment 173, 198-209.
652 Turner, A.J., Frankenberg, C. and Kort, E.A., 2019. Interpreting contemporary trends in
653   atmospheric methane. Proceedings of the National Academy of Sciences 116 (8),
654   2805-2813.
655 Turner, A.J. and Jacob, D.J., 2015. Balancing aggregation and smoothing errors in inverse models.
656   Atmos. Chem. Phys. 15 (12), 7039-7048.
657 Turner, A.J., Jacob, D.J., Wecht, K.J., et al., 2015. Estimating global and North American methane
658   emissions with high spatial resolution using GOSAT satellite data. Atmos. Chem. Phys. 15
659   (12), 7049-7069.

660 Veefkind, J.P., Aben, I., McMullan, K., et al., 2012. TROPOMI on the ESA Sentinel-5 Precursor: A
661   GMES mission for global observations of the atmospheric composition for climate, air
662   quality and ozone layer applications. Remote Sensing of Environment 120, 70-83.
663 Verhulst, K.R., Karion, A., Kim, J., et al., 2017. Carbon dioxide and methane measurements from
664   the Los Angeles Megacity Carbon Project – Part 1: calibration, urban enhancements, and
665   uncertainty estimates. Atmos. Chem. Phys. 17 (13), 8313-8341.
666 Wang, W., Tian, Y., Liu, C., et al., 2017. Investigating the performance of a greenhouse gas
667   observatory in Hefei, China. Atmos. Meas. Tech. 10 (7), 2627-2643.
668 Wunch, D., Toon, G.C., Blavier, J.-F.L., et al., 2011. The Total Carbon Column Observing Network.
669   Philosophical Transactions of the Royal Society A: Mathematical, Physical and
670   Engineering Sciences 369 (1943), 2087-2112.
671 Wunch, D., Toon, G.C., Wennberg, P.O., et al., 2010. Calibration of the Total Carbon Column
672   Observing Network using aircraft profile data. Atmos. Meas. Tech. 3 (5), 1351-1362.
673 Wunch, D., Toon, G. C., Sherlock, V., Deutscher, N. M., Liu, C., Feist, D. G., & Wennberg, P. O., 2015.
674   Documentation for the 2014 TCCON Data Release (GGG2014.R0). CaltechDATA.
675   https://doi.org/10.14291/TCCON.GGG2014.DOCUMENTATION.R0/1221662.
676 Yang, Y., Zhou, M., Langerock, B., et al., 2020. New ground-based Fourier-transform
677   near-infrared solar absorption measurements of XCO2, XCH4 and XCO at Xianghe,
678   China. Earth Syst. Sci. Data 12 (3), 1679-1696.
679 Yang, Y., Zhou, M., Wang, T., et al., 2021. Spatial and temporal variations of CO2 mole fractions
680   observed at Beijing, Xianghe, and Xinglong in North China. Atmos. Chem. Phys. 21 (15),
681   11741-11757.
682 Yin, Y., Chevallier, F., Ciais, P., et al., 2021. Accelerating methane growth rate from 2010 to 2017:
683   leading contributions from the tropics and East Asia. Atmos. Chem. Phys. 21 (16),
684   12631-12647.
685 Zeng, N., Han, P., Liu, Z., et al., 2021. Global to local impacts on atmospheric CO2 from the
686   COVID-19 lockdown, biosphere and weather variabilities. Environmental Research
687   Letters 17 (1), 015003.
688 Zhang, B., Yang, T., Chen, B. and Sun, X., 2016. China's regional CH4 emissions: Characteristics,
689   interregional transfer and mitigation policies. Applied energy 184, 1184-1195.
690 Zhang, G., Xiao, X., Dong, J., et al., 2020. Fingerprint of rice paddies in spatial–temporal dynamics
691   of atmospheric methane concentration in monsoon Asia. Nature Communications 11 (1),
692   554.
693 Zhao, X., Marshall, J., Hachinger, S., et al., 2019. Analysis of total column CO2 and CH4
694   measurements in Berlin with WRF-GHG. Atmos. Chem. Phys. 19 (17), 11279-11302.
695 Zhou, M., Langerock, B., Wang, P., et al., 2023. Understanding the variations and sources of CO,
696   C2H2, C2H6, H2CO, and HCN columns based on 3 years of new ground-based Fourier
697   transform infrared measurements at Xianghe, China. Atmos. Meas. Tech. 16 (2), 273-293.
698 Zhou, M.W., P.; Kumps, N.; Hermans, C.; Nan, W., 2022. TCCON Data from Xianghe, China,
699   Release GGG2020.R0. https://doi.org/10.14291/tccon.ggg2020.xianghe01.R0.
700